BIOMICROFLUIDICS **4**, 043008 (2010)

Optofluidic refractometer using resonant optical tunneling effect

A. Q. Jian,[1] X. M. Zhang,[1,a)] W. M. Zhu,[2] and M. Yu[3]
[1]*Department of Applied Physics, The Hong Kong Polytechnic University, Hung Hom, Kowloon, Hong Kong*
[2]*School of Electrical and Electronic Engineering, Nanyang Technological University, Nanyang Avenue, Singapore 639798*
[3]*Department of Mechanical Engineering, University of Maryland, College Park, Maryland 20742, USA*

(Received 31 July 2010; accepted 25 September 2010; published online 30 December 2010)

This paper presents the design and analysis of a liquid refractive index sensor that utilizes a unique physical mechanism of resonant optical tunneling effect (ROTE). The sensor consists of two hemicylindrical prisms, two air gaps, and a microfluidic channel. All parts can be microfabricated using an optical resin NOA81. Theoretical study shows that this ROTE sensor has extremely sharp transmission peak and achieves a sensitivity of 760 nm/refractive index unit (RIU) and a detectivity of 85 000 RIU^{-1}. Although the sensitivity is smaller than that of a typical surface plasmon resonance (SPR) sensor (3200 nm/RIU) and is comparable to a 95% reflectivity Fabry–Pérot (FP) etalon (440 nm/RIU), the detectivity is 17 000 times larger than that of the SPR sensor and 85 times larger than that of the FP etalon. Such ROTE sensor could potentially achieve an ultrahigh sensitivity of 10^{-9} RIU, two orders higher than the best results of current methods. © *2010 American Institute of Physics.* [doi:10.1063/1.3502671]

I. INTRODUCTION

Accurate measurement of refractive index (RI) of liquid samples is of great importance to many industrial processes and research studies.[1] Over the years, many refractometries have been developed and the sensitivity has been improved gradually from 10^{-2} to 10^{-7} refractive index unit (RIU). According to the working principles, most available methods could be roughly classified into three categories: geometrical optics, wave optics and near-field optics (nano-optics). The geometrical optics methods make use of the ray nature of the light and usually measure the refraction,[2] reflection,[3] and deflection[4,5] at the interface of the liquid sample and other reference media. As one of the most popular commercial refractometers, Abbé refractometer could reach 10^{-4} RIU by using the total internal reflection phenomenon. The wave optics based methods exploit the wave nature of light and mainly measure the RI by diffraction,[6] forward/backward scattering[7,8] and interference (e.g., Fabry–Pérot,[9–11] Mach–Zehnder,[12,13] double slits,[14] Michelson,[15] low coherence,[16] and fiber Bragg gratings[17,18]). These methods improve the sensitivity to 10^{-4}–10^{-6} RIU since the wavelength acts naturally as the absolute reference of length. Nowadays, the near-field optics methods, which make use of evanescent waves that exists in the subwavelength region near the interface of two medias, have attracted more and more interests. Inspired by the recent rapid progress of nanotechnology, different near-field mechanisms have been incorporated into the RI measurement, notably surface plasmon resonance (SPR),[19–21] whispering gallery modes of microresonators,[22] photonic bandgap waveguides,[23] photonic crystal

a)Author to whom correspondence should be addressed. Tel.: +852-3400-3258. FAX: +852-2333-7629. Electronic mail: apzhang@inet.polyu.edu.hk. Present Address: CD609, The Hong Kong Polytechnic University, Hung Hom, Kowloon, Hong Kong SAR, People's Republic of China.

fibers,[24] and local coupling of slab waveguides and tapered optical fibers.[25,26] As the near-field effect is confined to a subwavelength region, it intensifies the interaction and thus further improves the sensitivity to a level close to 10^{-7} RIU. However, currently the 10^{-7} RIU has become a formidable barrier, and none of the available methods is able to go beyond it.[7,27,28] On the other hand, the authors recently explored the resonant optical tunneling effect (ROTE) for optical switching functions[29] and found that it is extremely sensitive to the RI change, making it highly potential to break the current sensitivity barrier.

In this paper, the resonant optical tunneling effect will be exploited for ultrahigh sensitivity measurements of liquid RI using a microfluidic structure. The device design and the theoretical analysis will be elaborated. In this sensor, the RI can be retrieved by the change of transmission power or the shift of ROTE peak. The sensor performance such as sensitivity and detectivity will be investigated and compared with the Fabry–Pérot etalon and the SPR method. To the best knowledge of the authors, this is the first systematic theoretical study of the ROTE and also the first attempt to exploit the ROTE for sensor applications. On the most fundamental level, the refractive index varies according to the concentration of a solute in a solvent. The ultrahigh sensitivity promises a reliable and quantitative method to monitor the tiny change of the biochemical constituents (e.g., 10^{-9} RIU corresponds to approximately 1 fmol/l of salt in water). Further, the refractive index of a live cell is a valuable parameter for quantifying cell physiology and pathology.[30] This is particularly useful for drug screening and biomedical studies since the cells and other bioparticles could be monitored in real time and in their natural living states without the need for any biochemical marking, labeling, immobilizing, amplifying, or culturing processes.[31,32] The work would have a great impact on the environment protection, drinking water safety, and biomedical discoveries.

II. CONCEPT AND DEVICE DESIGN

The top view of the ROTE sensor design is shown in Fig. 1(a), which consists of two identical hemicylindrical prisms at two ends and a microfluidic channel in the middle separated by two air tunneling gaps. The whole structure sits on a substrate and may be encapsulated by another top cover (not shown in the figure). The microfluidic channel has a central channel and two channel walls for the liquid sample to flow through. The structure of this sensor has seven layers in total. The design parameters of sensor are listed in Table I. It is to be noted that the widths of the tunneling gap, channel wall, and channel are all normalized to the wavelength of incident light.

The optical model of the ROTE sensor is illustrated in Fig. 1(b). The incident light hits the interface between the first prism and the air tunneling gap at an angle greater than the critical angle, tunnels across the air gap, and propagates through the microchannel. It then passes another gap and reaches the prism to form the transmission output. The symmetry of the structures ensures a high coupling efficiency from the input to the output. The liquid sample follows through the microchannel and becomes part of the resonant tunneling structure, thus its RI would affect the transmission.

The corresponding quantum model is shown in Fig. 1(c). According to the relationship between the refractive index n and the optical potential V (Ref. 29) ($V=-n^2k_0^2$, where k_0 is the wavenumber), the high refractive index parts (the prisms, the channel walls, and the central channel) correspond to low optical potentials for the photons, while the low index parts (i.e., the two air tunneling gaps) produce high optical potentials and thus the optical barriers. From this model, the incoming photons tunnel through the first optical barrier and resonate between the two optical barriers before they tunnel again through the second optical barrier. This is how the resonant optical tunneling effect comes into being. The resonance condition is highly dependent on the optical path length $L=n_3g$, where n_3 is the RI of the central channel and g is the physical length of the central channel. Once the RI is changed, the resonance condition is broken; thus the transmission intensity will be reduced or the transmission peak will be shifted.

The microchannel structure can be fabricated by thiolene based resin NOA81 (Norland optical adhesive) instead of the widely used mirofluidic material polydimethylsiloxane (PDMS). NOA81 has an elastic modulus three orders of magnitude higher than PDMS (typically 1 GPa) and could

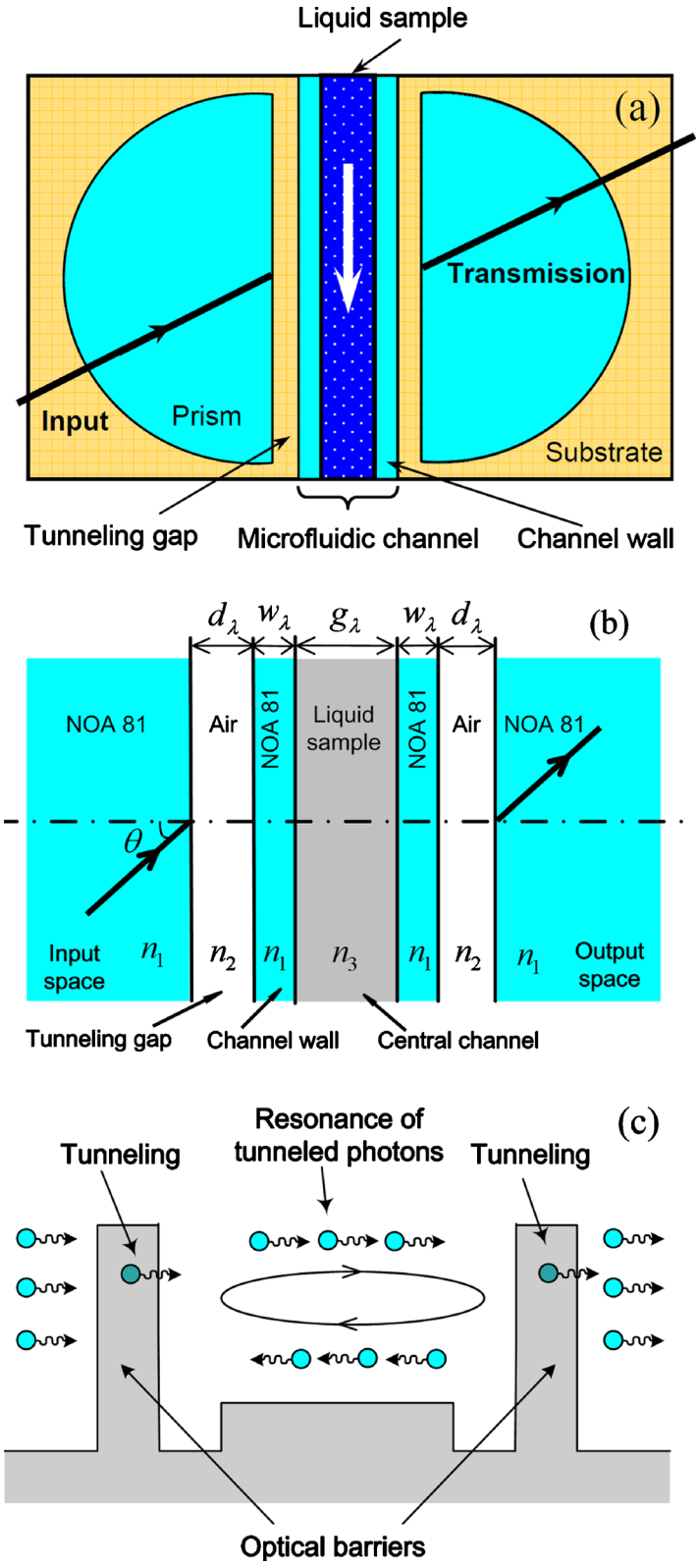

FIG. 1. Device design and theoretical models of the microfluidic refractive index sensor. (a) Top view of the sensor structure; (b) optical model of the sensor; and (c) equivalent quantum model of the sensor.

TABLE I. Design parameters of the refractive index sensor.

Parameter	Symbol	Values	
		S-pol.	P-pol.
Normalized tunneling gap	d_λ	1.5000	1.5000
Incident angle	θ	42.0233°	42.0738°
Normalized channel width	g_λ	20.6350	20.7955
Normalized width of channel walls	w_λ	5.000	5.000
Refractive index of prisms and channel walls	n_1	1.560	1.560
Refractive index of tunneling gap	n_2	1.000	1.000
Refractive index of liquid sample	n_3	1.330	1.330

fabricate pressure resistant devices for the transport of complex fluids.[33] This avoids sagging effects even for very low aspect ratio shallow channels. Moreover, NOA81 enables the replication of submicron features, low autofluorescence and biocompatibility, which is suitable for the sensor application. The refractive index of NOA81 is 1.56 from the datasheet. According to Table I, if the D-line emission (wavelength 589 nm) is used as the light source, the width of central channel is larger than 12 μm with over 3 μm channel wall. The high processing precision of NOA81 ensures that the all the design parameters could be achieved. A pair of single-mode optical fibers can be used for light input and output. The incident angle could be adjusted by high-precision micropositioner.

From the above discussion, it can be seen that the seven-layer ROTE sensor is similar to the five-layer structure that was studied by the authors previously, which had two prisms, two air gaps, and a central slab.[29] The difference is that the previous study used only one central slab in the middle, while the ROTE sensor has a three-layer microfluidic channel in the middle. This is because the ROTE sensor is designed for liquid samples; two channel walls have to be used to contain the liquid sample inside the central channel. As the liquid sample and the two channel walls have higher refractive indices than the air tunneling gaps, the whole microfluidic channel can be treated as a single layer. From this understanding, the combined effect of the central channel and the two channel walls is equivalent to the central slab in the previous study, and thus this seven-layer structure functions very similarly to the previous fix-layer structure in term of the ROTE.[29] This point is also supported by the illustration in Fig. 1(c); the channel walls and the central channel produce low optical potentials and do not act as optical barriers to the photons.

III. THEORETICAL ANALYSIS

To measure the RI using the ROTE sensor, there are two approaches: the intensity-based approach and the spectrum-based approach. The former uses a single-wavelength laser as the light source and monitors the change of transmission intensity, and the latter utilizes a broadband light source as the input and monitors the shift of transmission peak. Detailed analyses of these two approaches will be presented below after a brief presentation of the analytical method.

A. Transfer matrix method

According to Fig. 1(b), the sensor structure can be treated as a multilayer optical medium, and thus the transmission can be analyzed using the transfer matrix method (TMM), which is widely used for calculating the light propagation through a multilayer medium consisting of $(N-1)$ isotropic and homogeneous layers.[34] Each layer is called a slab, the slabs are numbered from 1 to $N-1$ from the input side to the output side, and the input space is numbered as 0, whereas the output space is as N. According to the TMM, when the light passes the slabs, the electric field vector and the magnetic field vector follow the relationship

$$\begin{bmatrix} E_N \\ H_N \end{bmatrix} = [M] \cdot \begin{bmatrix} E_0 \\ H_0 \end{bmatrix}, \tag{1}$$

where E_0 and H_0 are the electric field vector and the magnetic field vector on the input side (i.e., in the interface between the input space and the first slab), E_N and H_N are the electric field vector and the magnetic field vector on the output side [i.e., in the interface between the $(N-1)$th slab and the output space], and $[M]$ is the characteristic matrix of the multilayer structure as defined by

$$[M] = \begin{bmatrix} m_{11} & m_{12} \\ m_{21} & m_{22} \end{bmatrix} = M_{N-1} \cdots M_1 = \prod_{k=1}^{N-1} \begin{bmatrix} \cos\ \delta_k & \dfrac{i \sin\ \delta_k}{\eta_k} \\ i\eta_k \sin\ \delta_k & \cos\ \delta_k \end{bmatrix}, \tag{2}$$

where δ_k is the phase factor of the kth slab as given by

$$\delta_k = \frac{2\pi}{\lambda} n_k d_k \cos\ \theta_k = \frac{2\pi d_k}{\lambda} (\varepsilon_k - n_0^2 \sin^2\ \theta_0)^{1/2}. \tag{3}$$

The variable d_k is the thickness of the kth slab, θ_0 is the incident angle, λ is the wavelength, n_k is the refractive index with $n_k = (\varepsilon_k \mu_k)^{1/2}$, and ε_k and μ_k are the permittivity and permeability of the kth slab, respectively. The variable η_k is the optical admittance and has different forms for different polarization states; there are $\eta_k^s = (\varepsilon_k / \mu_k)^{1/2} \cos\ \theta_k = (\varepsilon_k - n_0^2 \sin^2\ \theta_0)^{1/2}$ for S-polarization and $\eta_k^p = (\varepsilon_k / \mu_k)^{1/2} (1/\cos\ \theta_k) = \varepsilon_k / \eta_k^s$ for P-polarization.

Finally, the transmission T of the entire multilayer structure can be written in terms of the Fresnel reflections (t_s and t_p) and the elements of the matrix M,

$$T_s = \frac{\eta_N^s}{\eta_0^s} |t_s|^2 = \frac{\eta_N^s}{\eta_0^s} \cdot \left| \frac{2\eta_0^s}{(m_{11}^s + m_{12}^s \cdot \eta_N^s)\eta_0^s + (m_{21}^s + m_{22}^s \cdot \eta_N^s)} \right|^2, \tag{4}$$

$$T_p = \frac{\eta_N^p}{\eta_0^p} |t_p|^2 = \frac{\eta_N^p}{\eta_0^p} \cdot \left| \frac{2\eta_0^p}{(m_{11}^p + m_{12}^p \cdot \eta_N^p)\eta_0^p + (m_{21}^p + m_{22}^p \cdot \eta_N^p)} \right|^2. \tag{5}$$

Here, the S-polarization means the electric field is always perpendicular to the incident plane; it can be also called as the transverse electric (TE) polarized light. Similarly, the P-polarization means the electric field is always inside the incident plane and is the same as the transverse magnetic (TM) polarized light.

B. Intensity-based refractive index sensing

This part will study the dependence of the transmission on the structural parameters and the RI change. The designed parameters as listed in Table I. From Fig. 1(a), one can imagine that the liquid sample could flow through the central channel or the tunneling gaps. Therefore, it is necessary to study which one has better sensitivity to the physical size and the RI.

The transmissions of both S- and P-polarizations are contoured in Fig. 2 with respect to the channel width and the tunneling gap. The bright region corresponds to high transmission. As can be observed in Figs. 2(a) and 2(b), a spike of bright band appears upward for both P-polarization and S-polarization. Near the spike, a small change of the central channel width would cause a large variation of the transmission (from bright to dark). However, with the change of the tunneling gap, the transmission is always in the bright region and thus does not vary that much. This shows clearly that the transmission is far more sensitive to the width of central channel than to that of tunneling gap. The transmission has different levels of dependence on the RI changes of different parts. Figure 3 shows the contoured transmissions with respect of the RI changes of the central channel (Δn_3, the x axis) and the tunneling gap (Δn_2, the y axis). Both contours have bright bands in the vertical direction. The transmissions vary more rapidly along the x axis than along the y axis for both P-polarization and S-polarization, which suggests that the transmission is more

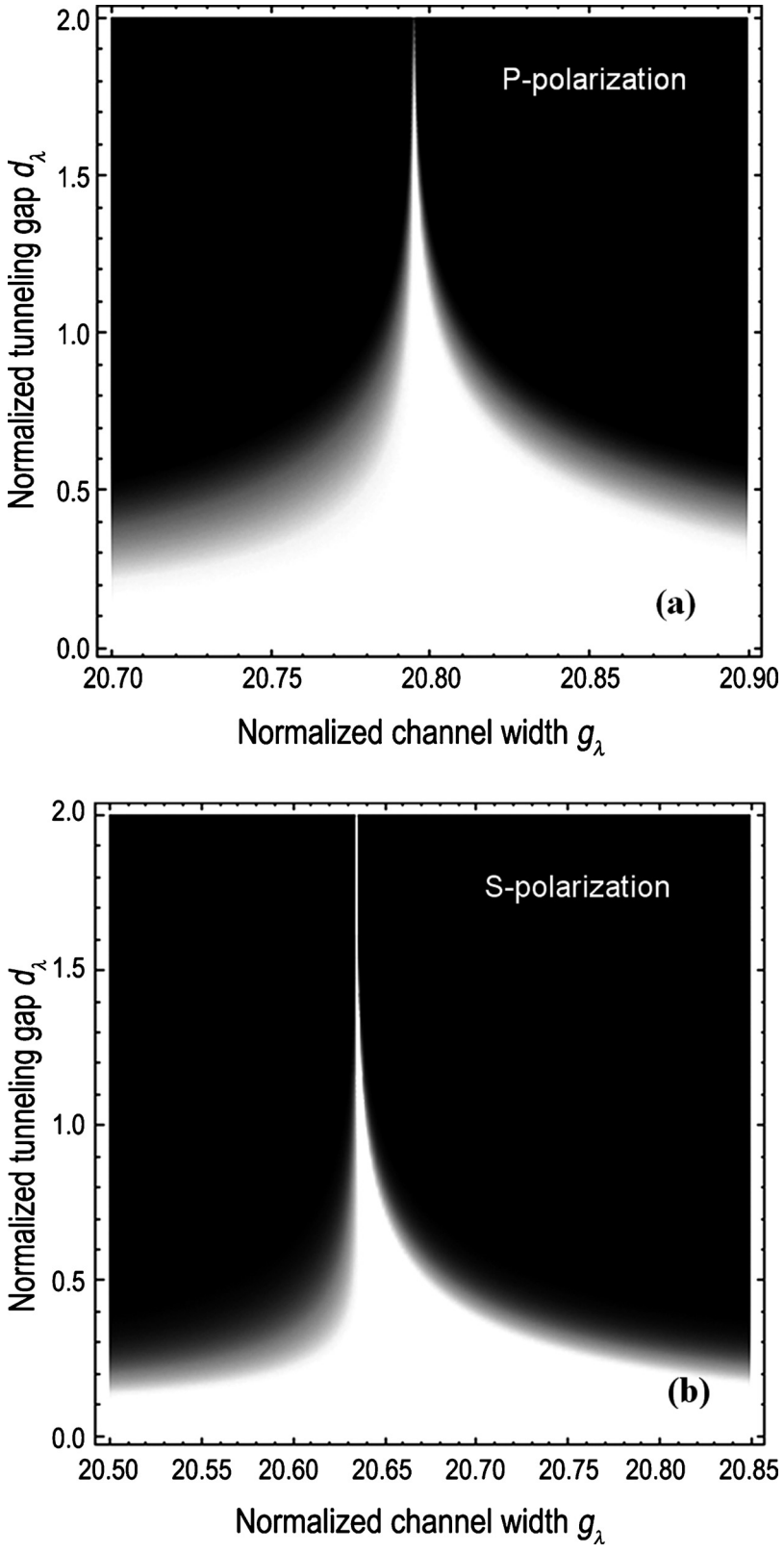

FIG. 2. Contours of the transmission with respect to the central channel width and the tunneling gap for (a) P-polarization and (b) S-polarization.

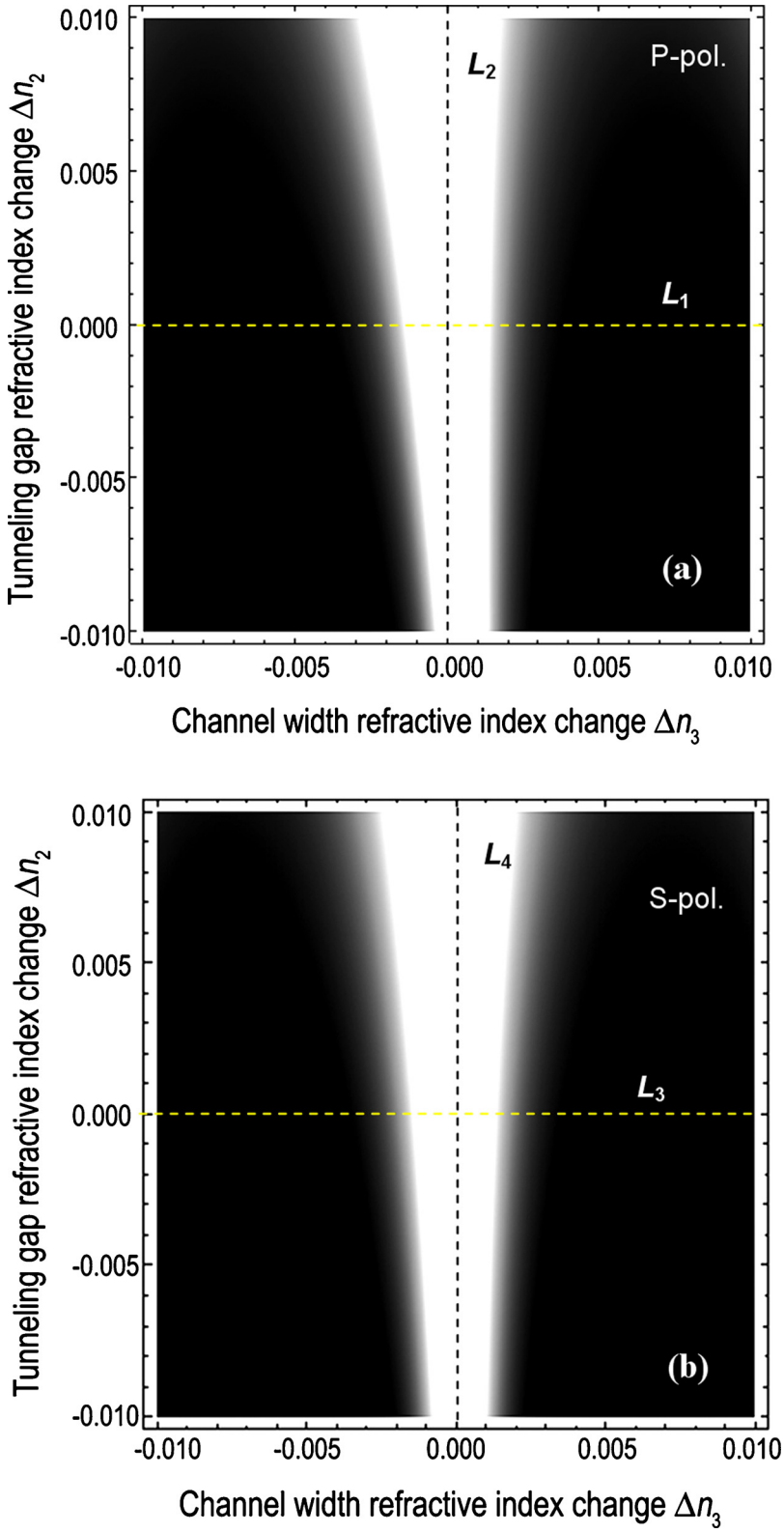

FIG. 3. Transmissions contoured with respect of the refractive index changes of the central tunnel channel and the tunneling gap for (a) P-polarization and (b) S-polarization.

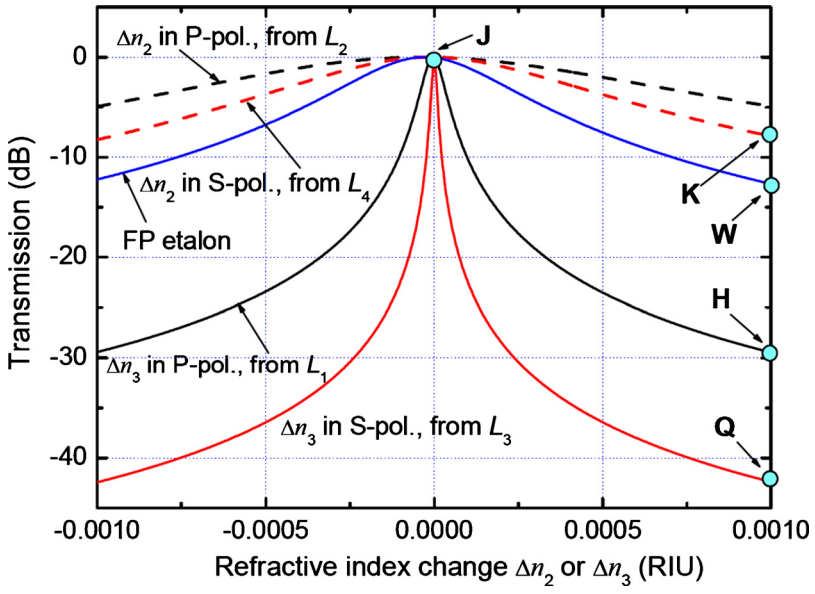

FIG. 4. The independence of transmission on the changes of refractive indices of the central tunnel channel (Δn_3) and the tunneling gap (Δn_2) for P-polarization (black lines) and S-polarization (red lines). The curves are obtained from the observation line L_1 to L_4 in Fig. 3. For comparison, the transmission of a FP etalon ($R=0.95$) is also plotted.

sensitive to the RI change of the central channel than to that of tunneling gap. Quantitative comparison can be obtained by plotting the transmission curves along the observation lines L_1 to L_4 (see Fig. 3). The plotted results are shown in Fig. 4. It is easy to see that the transmission drops much faster with Δn_3 than Δn_2. At the initial state (point J), the transmission is at 0 dB (i.e., 100% transmission). For $\Delta n_3 = 1 \times 10^{-3}$ RIU, the transmission of the S-polarization state is reduced to -42.4 dB (point Q), while for $\Delta n_2 = 1 \times 10^{-3}$ RIU, it drops to only -8.3 dB (point K). Therefore, the transmission is over 1000 times more sensitive to the refractive index change of the central channel than to that of the tunneling gap. For this reason, the liquid sample is designed to flow through the central channel rather than the tunneling gap.

The influence of the polarization state can also be derived from Fig. 4. Comparing the two curves of Δn_3 (those from L_1 and L_3), it can be seen that the S-polarization experiences a steeper drop of the transmission than the P-polarization. For instance, at $\Delta n_3 = 1 \times 10^{-3}$ RIU, the transmission is -42.4 dB for the S-polarization (point Q), whereas it is only -29.3 dB for the P-polarization (point H). Therefore, the ROTE sensor can be >10 times more sensitive when the S-polarization is used. For this reason, the analysis below will always use the S-polarization.

To show the ultrahigh sensitivity of the ROTE sensor, the transmission variation of a Fabry–Pérot (FP) etalon with 95% reflectivity mirrors is also plotted in Fig. 4. The length of the FP resonant cavity is 33.6λ, which is chosen the same as the ROTE region's effect length [i.e., channel width+2×(channel wall width+tunneling gap width)]. At $\Delta n_3 = 1 \times 10^{-3}$ RIU, the FP transmission drops to only -12.2 dB, three orders smaller than the drop of -42.4 dB in the ROTE sensor. As the etalons have already demonstrated a sensitivity of 10^{-4}–10^{-6} RIU,[35] it is reasonable to expect the ROTE sensor achieves an unprecedented level of sensitivity up to 10^{-7}–10^{-9} RIU.

The above analysis uses a single-wavelength laser as the input and finds rapid drop of the transmission when the parameters of the central channel moves away from the designed values. Such intensity-based approach requires high fidelity of fabrication and strict control of experimental conditions (such as the initial RI of the liquid sample, temperature, etc.), making it challenging in real implementation. Such problem could be circumvented by using a broadband light source as the input and then by observing the transmission peak. Because the dimensions of this ROTE sensor structure are normalized to the wavelength in the calculation, the broadband of light source

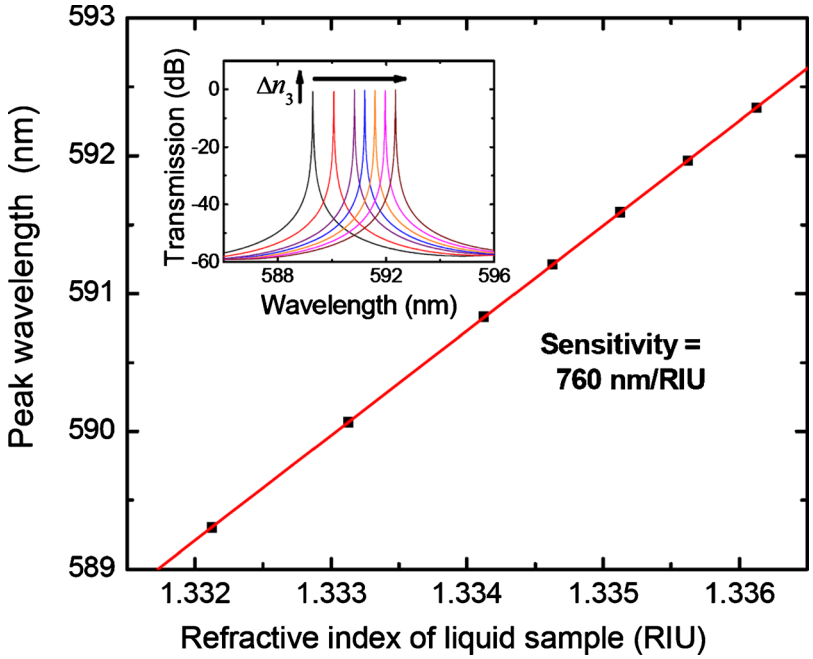

FIG. 5. Shift of the transmission peak wavelength with respect to the refractive index n_3 of the liquid sample in the central channel. The inset illustrates the shift of transmission peak with the increase of the refractive index n_3.

can easily offset the fabrication error and the drift of experimental conditions by a shift of the transmission peak. In addition, it makes the experimental observation easier since there is always a peak in the output spectrum. More details are presented in the following part.

C. Spectrum-based refractive index sensing

Assume that the incident broadband light has a central wavelength of 589 nm (D-line emission of a sodium lamp) and a bandwidth of 10 nm, the relationship between the peak shift and the RI change of the liquid sample in the central channel is plotted in Fig. 5. The inset shows the actual spectra correspond to the different RI of the liquid sample. The increase of the liquid sample RI causes a shift of the ROTE peak toward longer wavelength. The sensitivity of sensor obtained is 760 nm/RIU. With a high-resolution optical spectrum analyzer (0.01 picometer), the sensitivity of the ROTE senor could reach 1×10^{-8} RIU, roughly the same level as that of the intensity-based approach.

It should be noted that the shift of peak wavelength is not the only factor that determines the sensitivity of a sensor, the spectral width of the transmission peak is equally important. Some other methods such as the SPR sensors and the short-cavity FP etalons could produce very large wavelength shift in response to the RI change. However, the peak (or dip) has rather large spectral width, making it difficult to find the accurate position of peak (or dip), especially in the presence of strong noise. Here, we propose a parameter with more reference value—*detectivity*, which is defined as

$$\text{detectivity} = \frac{\delta\lambda}{\delta\lambda_{0.5}} \frac{1}{\Delta n}, \tag{6}$$

where $\delta\lambda$ is the wavelength shift in response to the RI change Δn and $\delta\lambda_{0.5}$ is the 3 dB spectral width of the spectrum. The detectivity is based on the parameter signal-to-noise ratio proposed in some previous studies.[36,37]

Figure 6 compares the spectra of the ROTE sensor with the FP etalon and the SPR sensor. The latter two have been well established for high sensitivity RI measurement. The parameters of FP

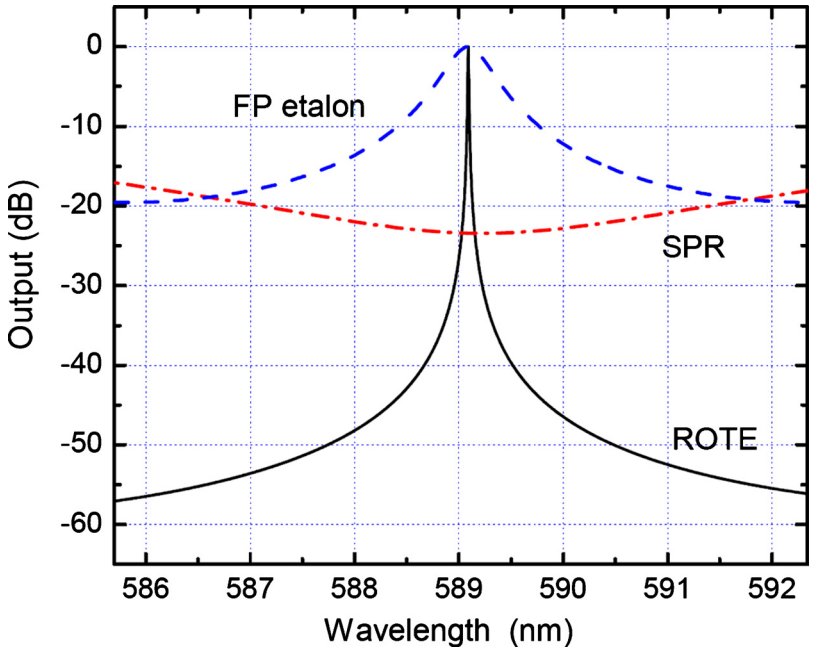

FIG. 6. Comparison of the transmission spectrum of the ROTE sensor with the transmission spectrum of the FP etalon and the reflection spectrum of SPR sensors. The latter two are widely used for highly sensitive refractive index sensing.

etalon are the same as mentioned above. The SPR spectrum is calculated using the parameters from Ref. 37. The SPR sensor utilizes a 50 nm thick gold thin film coated on the surface of NOA81 and has the incident light entering at 70°. It can be seen from Fig. 6 that the ROTE sensor has much narrower spectral width than the FP etalon and the SPR sensor. The sensitivities and the detectivities of the different sensors are listed in Table II. In terms of sensitivity, the SPR has the largest sensitivity of 3200 nm/RIU, about 4.2 times of the ROTE sensitivity (760 nm/RIU) and 7.3 times of the FP etalon sensitivity (440 nm/RIU). Nevertheless, in terms of detectivity, the ROTE sensor obtains 85 000 RIU^{-1}, which is 85 times larger than the FP etalon (1000 RIU^{-1}) and 17 000 times larger than the SPR sensor ($\sim$5 RIU^{-1}). This comparison gives great confidence that the ROTE sensor can achieve an unprecedented sensitivity of RI measurement.

IV. CONCLUSIONS

This paper aims to break the current sensitivity limit of 10^{-7} RIU in measuring the liquid refractive index by exploiting a special physical mechanism of resonant optical tunneling effect. Theoretical study shows that the sensor has much higher detectivity than the well established methods such as Fabry–Pérot etalons and surface plasmon resonance sensors. It could achieve an ultrahigh sensitivity of up to 10^{-9} RIU. This is particularly useful for drug screening and biomedical studies.

TABLE II. Comparison of the sensitivity and detectivity of the ROTE sensor, the Fabry–Pérot etalon, and the SPR sensor (Ref. 37).

	ROTE sensor	FP etalon (R=95%)	SPR sensor
Sensitivity (nm/RIU)	760	440	3200
Detectivity (RIU^{-1})	85 000	1000	$\sim$5

ACKNOWLEDGMENTS

X.M.Z. acknowledges the fund support of Hong Kong Polytechnic University through Grant Nos, A-PD1S, G-YH81, and 1-ZV5K. M.Y. gratefully acknowledges the support received from U.S. National Science Foundation (Grant No. CMMI1031331).

[1] F. Vollmer and S. Arnold, Nat. Methods **5**, 591 (2008).
[2] D. Brennan, P. Lambkin, and P. Galvin, Meas. Sci. Technol. **19**, 085403 (2008).
[3] C. B. Kim and C. B. Su, Meas. Sci. Technol. **15**, 1683 (2004).
[4] F. Samedov, Opt. Laser Technol. **38**, 28 (2006).
[5] J. R. Majer, Talanta **23**, 747 (1976).
[6] A. Sabatyan and M. T. Tavassoly, Opt. Laser Technol. **41**, 892 (2009).
[7] D. Markov, D. Begari, and D. J. Bornhop, Anal. Chem. **74**, 5438 (2002).
[8] N. Burggraf, B. Krattiger, A. J. de Mello, N. D. de Rooij, and A. Manz, Analyst (Cambridge, U.K.) **123**, 1443 (1998).
[9] L. K. Chin, A. Q. Liu, C. S. Lim, C. L. Lin, T. C. Ayi, and P. H. Yap, Biomicrofluidics **4**, 024107 (2010).
[10] X. J. Liang, A. Q. Liu, C. S. Lim, T. C. Ayi, and P. H. Yap, Sens. Actuators, A **133**, 349 (2007).
[11] W. Z. Song, X. M. Zhang, A. Q. Liu, C. S. Lim, P. H. Yap, and Habib Mir M. Hosseini, Appl. Phys. Lett. **89**, 203901 (2006).
[12] A. Banerjee, S. Mukherjee, R. K. Verma, B. Jana, T. K. Khan, M. Chakroborty, R. Das, S. Biswas, A. Saxena, V. Singh, R. M. Hallen, R. S. Rajput, P. Tewari, S. Kumar, V. Saxena, A. K. Ghosh, J. John, and P. Gupta-Bhaya, Sens. Actuators B **123**, 594 (2007).
[13] J. Hilton, Phys. Educ. **4**, 56 (1969).
[14] G. H. Cross, A. A. Reeves, S. Brand, J. F. Popplewell, L. L. Peel, M. J. Swann, and N. J. Freeman, Biosens. Bioelectron. **19**, 383 (2003).
[15] Z. Tian, S. S.-H. Yam, and H.-P. Loock, Opt. Lett. **33**, 1105 (2008).
[16] P. H. Tomlins, P. Woolliams, C. Hart, A. Beaumont, and M. Tedaldi, Opt. Lett. **33**, 2272 (2008).
[17] W. Liang, Y. Huang, Y. Xu, R. K. Lee, and A. Yariv, Appl. Phys. Lett. **86**, 151122 (2005).
[18] G. M. Rego, J. L. Santos, and H. M. Salgado, Opt. Commun. **259**, 598 (2006).
[19] X. Wu, J. Zhang, J. Chen, C. Zhao, and Q. Gong, Opt. Lett. **34**, 392 (2009).
[20] B. Lee, S. Roh, and J. Park, Opt. Fiber Technol. **15**, 209 (2009).
[21] G. J. Veldhuis and P. V. Lambeck, Appl. Phys. Lett. **71**, 2895 (1997).
[22] M. Ghulinyan, A. Pitanti, G. Pucker, and L. Pavesi, Opt. Express **17**, 9434 (2009).
[23] J. Wu, D. Day, and M. Gu, Appl. Phys. Lett. **92**, 071108 (2008).
[24] D. K. C. Wu, B. T. Kuhlmey, and B. J. Eggleton, Opt. Lett. **34**, 322 (2009).
[25] O. S. Wolfbeis, Anal. Chem. **78**, 3859 (2006).
[26] S. Campopiano, R. Bernini, L. Zeni, and P. M. Sarro, Opt. Lett. **29**, 1894 (2004).
[27] D. Monzón-Hernández and J. Villatoro, Sens. Actuators B **115**, 227 (2006).
[28] Y. L. Hoo, W. Jin, L. Xiao, J. Ju, and H. L. Ho, Sens. Actuators B **136**, 26 (2009).
[29] W. M. Zhu, X. M. Zhang, A. Q. Liu, H. Cai, T. Jonathan, and T. Bourouina, Appl. Phys. Lett. **92**, 251101 (2008).
[30] G. Mazarevica, T. Freivalds, and A. Jurka, J. Biomed. Opt. **7**, 244 (2002).
[31] V. S.-Y. Lin, K. Motesharei, K.-P. S. Dancil, M. J. Sailor, and M. R. Ghadiri, Science **278**, 840 (1997).
[32] T. P. Burg, M. Godin, S. M. Knudsen, W. Shen, G. Garlson, J. S. Foster, K. Babcock, and S. R. Manalis, Nature (London) **446**, 1066 (2007).
[33] D. Bartolo, G. Degre, P. Nghe, and V. Studer, Lab Chip **8**, 274 (2008).
[34] P. Yeh, *Optical Waves in Layered Media* (Wiley, New York, 1988).
[35] C. Monat, P. Domachuk, and B. J. Eggleton, Nature Photon. **1**, 106 (2007).
[36] A. K. Sharma and B. D. Gupta, Photonics Nanostruct. Fundam. Appl. **3**, 30 (2005).
[37] A. K. Sharma and B. D. Gupta, Nanotechnology **17**, 124 (2006).